Applied Surface Science 355 (2015) 1306–1315

Contents lists available at ScienceDirect

Applied Surface Science

journal homepage: www.elsevier.com/locate/apsusc

On the surface characteristics of a Zr-based bulk metallic glass processed by microelectrical discharge machining

Hu Huang, Jiwang Yan*

Department of Mechanical Engineering, Keio University, Yokohama 223-8522, Japan

ARTICLE INFO

Article history:
Received 16 July 2015
Received in revised form 26 August 2015
Accepted 27 August 2015
Available online 31 August 2015

Keywords:
Bulk metallic glass
Micro-electrical discharge machining
Surface characteristic
Crystallization

ABSTRACT

Microelectrical discharge machining (micro-EDM) performance of a Zr-based bulk metallic glass was investigated experimentally. Various discharge voltages and capacitances were used to study their effects on the material removal rate, cross-sectional profile, surface morphology and roughness, carbonization, and crystallization. Experimental results indicated that many randomly overlapped craters were formed on the EDMed surfaces, and their size and distribution were strongly dependent of the applied voltage and capacitance as well as their positions (center region or outer region), which further affected the surface roughness. Raman spectra and energy dispersive X-ray spectroscopy demonstrated that amorphous carbons originating from the decomposition of the EDM oil were deposited on the EDMed surface. Although some small sharp peaks appeared in the X-ray diffraction patterns of the micro-EDMed surfaces, a broad hump was maintained in all patterns, suggesting a dominant amorphous characteristic. Furthermore, crystallization was also affected by experimental conditions and machining positions. Results in this study indicate that micro-EDM under low discharge energy is useful for fabricating bulk metallic glass microstructures or components because of the ability to retain an amorphous structure.

1. Introduction

Because of their high elasticity, hardness, fracture toughness, and superior corrosion resistance, bulk metallic glasses (BMGs) are attractive materials for high-end products and high value-added metal components such as electronic frames, sport products, precision surgical instruments, and micro-electro-mechanical devices [1]. However, BMGs also exhibit some shortcomings such as very limited microscopic plasticity followed by catastrophic failure, dimensional limitations (difficult to produce large BMGs), relatively high cost resulting from expensive raw materials and subsequent shaping, which limit their widespread applications. To explore BMGs with enhanced plasticity and larger dimensions, lots of studies have been performed to investigate their preparation, structure, and mechanical properties as well as structure–property relationships, resulting in the development of many kinds of BMGs [2–7].

Compared to studies on the preparation, structure, and mechanical properties of BMGs, there are only a few studies that have focused on the machining and shaping abilities of BMGs, although it is very important and necessary from an application point of view. Bakkal et al. [8–15] studied the machining performance of a Zr-based BMG under various turning and drilling process parameters, such as chip formation, characteristics, surface roughness, cutting forces, tool wear, burr formation, oxidation, and crystallization. It was reported that BMG chips generated very bright light emission when a threshold cutting speed was applied, which was related to the oxidation of the Zr element because of the high chip temperature. Although high dimensional accuracy and surface roughness can be obtained by conventional machining methods, tool wear, burr formation, possible oxidation, and crystallization during high speed machining are still challenges. Furthermore, the difficulty in forming complex shapes, waste of a lot of materials compared to the small workpiece formed, and the difficulty in machining hard-brittle BMGs such as Fe-based BMGs are also big problems for conventional machining methods.

Compared to conventional machining methods, die-casting and some thermoplastic shaping methods of BMGs in the supercooled liquid region [16–25] show a great potential for scientific studies and commercial applications. Via these net-shape methods, many high value-added precision components have been formed such as micro-gears, tweezers, scalpels, golf clubs, and metallic glass cell phone casings. However, the high cost, limited mold-tool lifetimes, die-casting defects, and crystallization issues (hard to control the forming temperature, especially for BMGs having a narrow supercooled liquid region) remain problems to be solved for the widespread applications of these methods [1,19]. Hence, suitable

* Corresponding author.
E-mail addresses: huanghu@keio.jp (H. Huang), yan@mech.keio.ac.jp (J. Yan).

http://dx.doi.org/10.1016/j.apsusc.2015.08.239
0169-4332/

machining and shaping methods are greatly desired for the commercial applications of BMGs.

As a typical non-conventional machining method, electrical discharge machining (EDM) has been widely used to form deep and three-dimensional complex structures in die- and mold-making industry because of its high machining flexibility. It can machine various types of materials, especially hard-brittle materials [26–28], and also rough machining and fine machining can be performed by EDM. However, up to now, there have been few investigations on the machining performance of BMGs by EDM. EDM is an electro-thermal process involving material heating, melting, vaporization, and re-solidification. BMGs are also temperature sensitive. If unsuitable heating and cooling processes are experienced by the part, crystallization will occur, which lowers mechanical and chemical property advantages of BMGs. Conventional EDM employs a very high discharge energy resulting in significant melting and vaporization of the workpiece surface and forms a large heat affected zone (HAZ). In Ref. [29], many sharp peaks were observed in the X-ray diffraction (XRD) patterns of the EDMed surface of a Zr-based BMG, indicating that significant crystallization occurred. Compared to conventional EDM, micro-EDM may be a good choice to machine BMGs while maintaining their amorphous characteristics because of its relatively small discharge energy. Using comparative experiments, Yeo et al. [30] investigated the effects of machining conditions on the surface roughness, burr formation, and tool wear during micro-EDM of a Zr-based BMG. Chen et al. [31] studied the machining performance of micro-holes on three types of BMGs during micro-EDM, and they suggested that no crystallization occurred for these BMGs by measuring the indentation hardness around the machined holes. However, no direct evidence was provided. Up to now, the crystallization of BMGs during micro-EDM has been rarely discussed. In this study, we systematically investigated the micro-EDM machining performance of a Zr-based BMG by orthogonal experiments. The effects of the discharge voltage and capacitance on the material removal rate, cross-sectional profile, surface morphology, and roughness were studied first. After that, the emphasis was on the carbonization and crystallization of the EDMed surfaces of the BMG.

2. Materials and experiments

2.1. Materials

A $Zr_{41.2}Ti_{13.8}Cu_{12.5}Ni_{10}Be_{22.5}$ BMG sample with a diameter of 10 mm and thickness of 2 mm was cut from a bar using a low speed diamond saw, and then, mechanically polished using 400, 800, and 1500 grit sand papers in sequence. This BMG is commonly called Vitreloy 1, and its preparation processing and mechanical and physical properties have been well studied in literature (e.g., [32–36]). The main thermo-physical properties of Vitreloy 1 are listed in Table 1.

Table 1
Thermo-physical properties of $Zr_{41.2}Ti_{13.8}Cu_{12.5}Ni_{10}Be_{22.5}$ (Vitreloy 1).

Property	Condition	Value	References
Onset temperature of glass transition (K)	Heating rate, 40 K/min	637	[36]
Onset temperature of crystallization (K)	Heating rate, 40 K/min	733	[36]
Supercooled liquid region (K)	Heating rate, 40 K/min	96	[36]
Liquidus temperature (K)		993	[32]
Thermal conductivity (W/(m k))		4	[37]

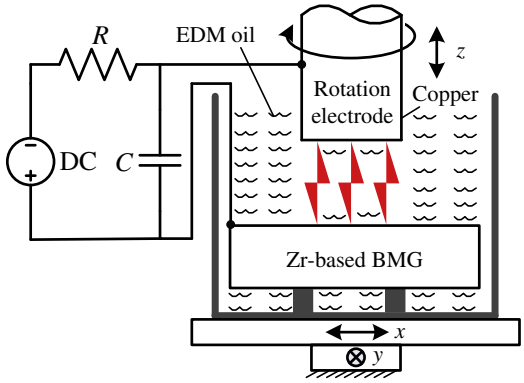

Fig. 1. Schematic diagram of the EDM experimental setup.

2.2. Micro-EDM experiments

EDM of the BMG was performed using a precision micro-EDM machine (Panasonic MG-ED72, Japan), which has a resistor–capacitor (RC) discharge circuit with a stepping resolution of 0.1 μm. Fig. 1 illustrates the schematic diagram of the EDM experimental setup. A copper rod was used as the tool electrode. For each micro-EDM experiment, the same machining depth of 0.1 mm was set with a feed rate of 5 μm/s and a rotational speed of 3000 rpm. Three voltages, 70 V, 90 V, and 110 V, and three capacitances, 220 pF, 1000 pF, and 3300 pF, were selected for the orthogonal experiments. EDM oil, CASTY-LUBE EDS, was used as the dielectric fluid. The experimental conditions are summarized in Table 2.

2.3. Characterization

After micro-EDM, the BMG sample was cleaned using alcohol. A laser probe (MP-3, Mitaka Kohki, Japan) was used to measure the profiles of the machined holes, and the three-dimensional topographies and surface roughness around the center region of the EDMed holes were tested using a white-light interferometer (CCI 1000, Taylor Hobson, UK). A thermal field emission scanning electron microscope (FE-SEM) (JSM-7600F, JEOL, Japan) was used to observe the microstructures of the EDMed holes. Carbonization and crystallization of the EDMed surfaces were characterized using an X-ray diffractometer (XRD, D8 Discover, Bruker, Germany), energy dispersive X-ray (EDX) spectroscopy (Bruker AXS, Germany), and laser micro-Raman spectroscopy (NRS-3100, JASCO, Japan).

3. Results and discussion

3.1. Material removal rate

By measuring the consumption time for each EDM experiment, the material removal rate (MRR) (the set value of machining depth divided by the time) at various voltages and capacitances were calculated and are presented in Fig. 2. For the same voltage, the

Table 2
Experimental conditions used for micro-EDM in this study.

Workpiece material	$Zr_{41.2}Ti_{13.8}Cu_{12.5}Ni_{10}Be_{22.5}$
Electrode material	Copper
Polarity	Positive (workpiece)
	Negative (tool)
Rotational speed (rpm)	3000
Feed rate (μm/s)	5
Voltage (V)	70, 90, 110
Condenser capacitance (pF)	220, 1000, 3300
Dielectric fluid	EDM oil (CASTY-LUBE EDS)

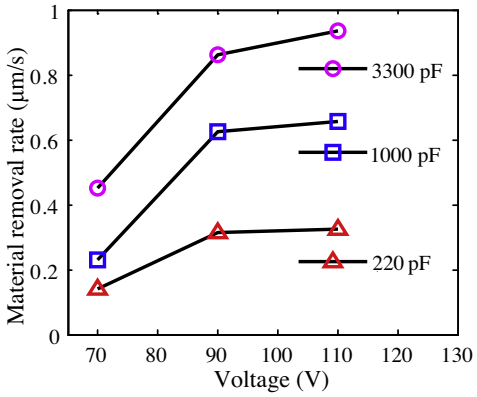

Fig. 2. Material removal rate at various voltages and capacitances.

MRR increases with increase in the capacitance, and the same phenomenon occurs with increased voltage for the same capacitance. The discharge energy E during pulse-on time is expressed as

$$E = \frac{1}{2}CV^2 \quad (1)$$

where C and V are the capacitance and voltage, respectively. According to the energy law in Eq. (1), results in Fig. 2 are reasonable because a higher discharge energy is generated at increased voltages and capacitances, which increases the MRR.

3.2. Cross-sectional profile

Fig. 3 illustrates the cross-sectional profiles of the EDMed holes. All the holes exhibit a tapered rather than perpendicular shape. Following the machining sequence, with the voltage changing from 110 V to 70 V, the tapered shape becomes more significant (Fig. 3a–c) because of the accumulated wear of the tool electrode. Compared to the holes machined at voltages of 110 V and 90 V, the holes obtained at 70 V show a depth closest to the set value of 0.1 mm, which demonstrates better depth replication and low tool electrode wear rate in the depth direction because of the low discharge energy.

3.3. Surface topography and roughness

Fig. 4 presents the three-dimensional topographies and surface roughness around the center region of the EDMed holes at various voltages and capacitances. The measured region is a 360 μm × 360 μm. Different colors denote different depths. Corresponding to the profiles in Fig. 3, deeper and wider pits are observed for the EDMed holes at a voltage of 70 V, compared to those at 110 V. For the same voltage, for example, 110 V, the EDMed surface becomes smoother with a decrease in the capacitance, exhibiting a decreased surface roughness from 351.425 nm to 196.553 nm corresponding to a capacitance change from 3300 pF to 220 pF. Similarly, for the same capacitance of 3300 pF, the surface roughness decreases from 351.425 nm to 305.320 nm with a decrease in the voltage from 110 V to 70 V. However, for capacitances of 1000 pF and 220 pF, the voltage change from 110 V to 90 V has a small impact on the measured surface roughness, although it decreased again, when the voltage was reduced to 70 V.

3.4. Surface morphology

To further explore the microstructures on the EDMed surfaces, high resolution FE-SEM was used to observe the EDMed holes. Fig. 5

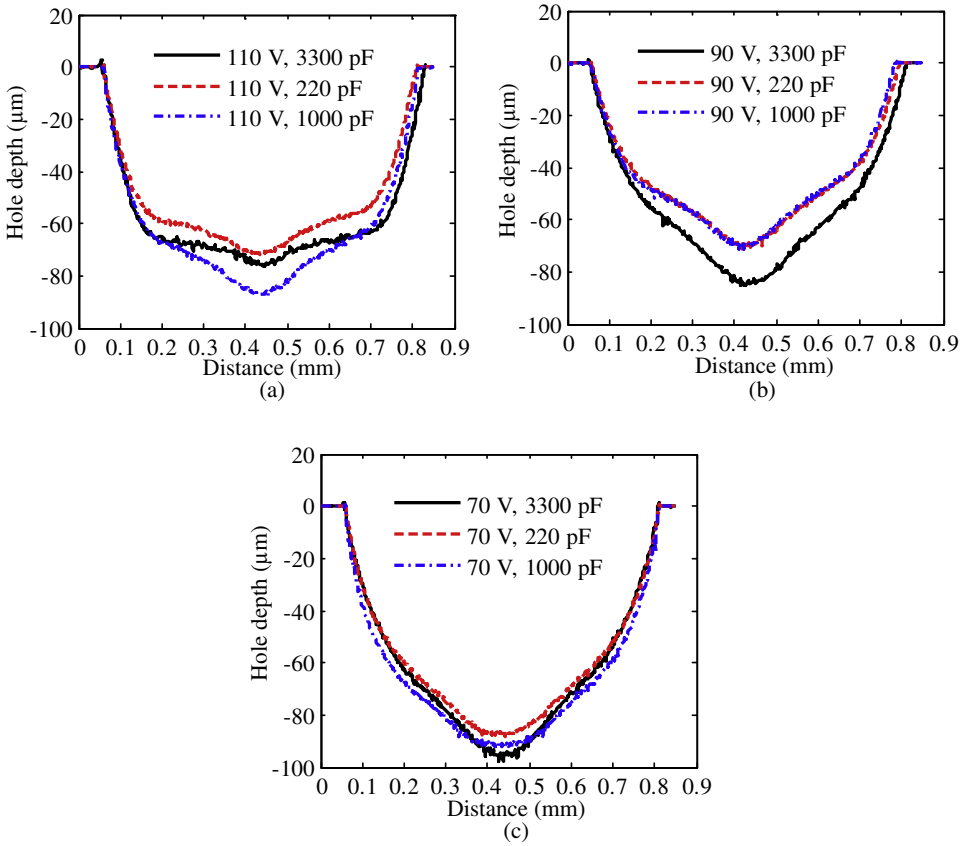

Fig. 3. Cross-sectional profiles of the EDMed holes at various voltages and capacitances: (a) 110 V, (b) 90 V, (c) 70 V.

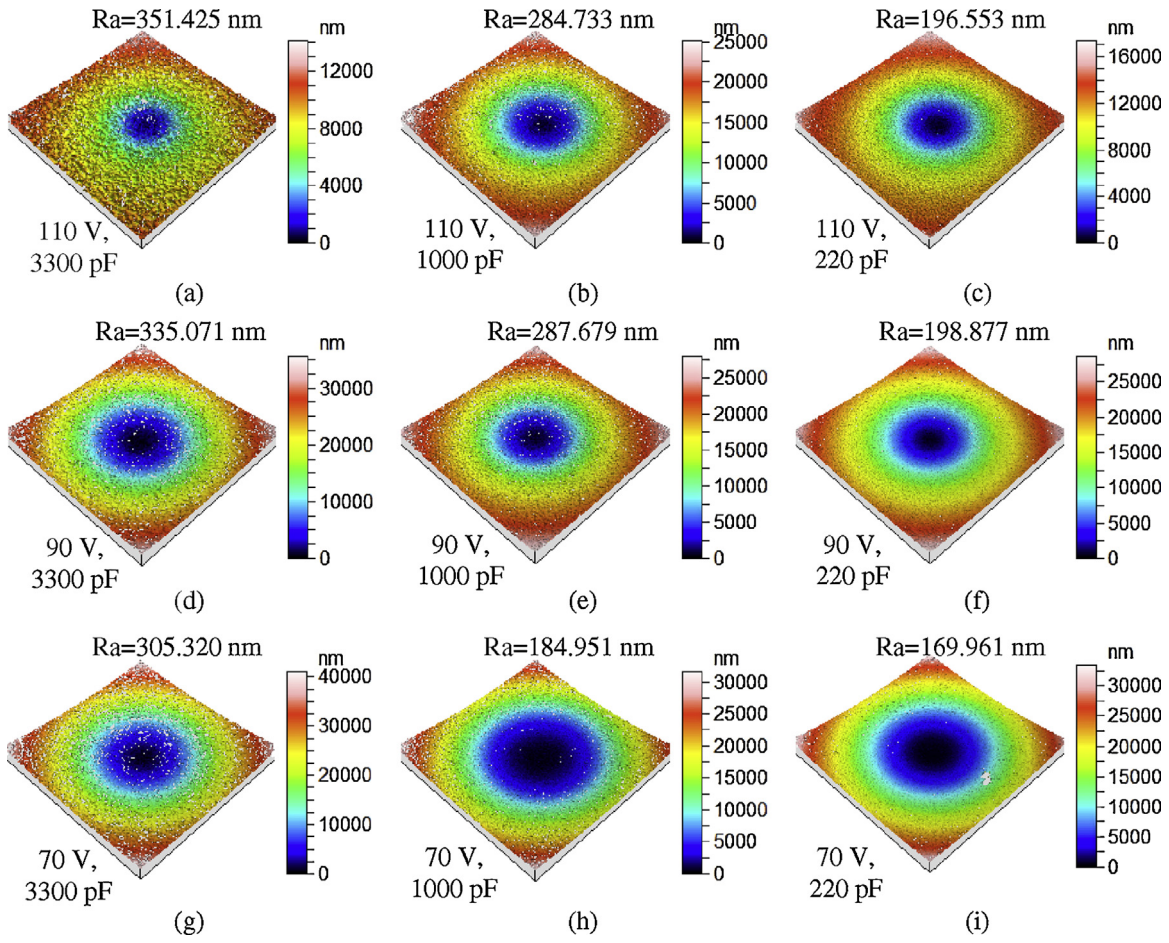

Fig. 4. Three-dimensional topographies and surface roughness around the center region of the EDMed holes at various voltages and capacitances: (a)–(c) 110 V, (d)–(f) 90 V, (g)–(i) 70 V. (For interpretation of the references to color in this figure text, the reader is referred to the web version of this article.)

presents the surface morphologies of the EDMed holes at a voltage of 90 V and various capacitances. For comparative analysis, Fig. 6 shows the surface morphologies of the EDMed holes at a capacitance of 3300 pF and voltages of 110 V and 70 V. In Fig. 5, the recast layer is observed at the edge of the holes, and its width is obviously decreased with a decrease in the capacitance. Inside the holes, many randomly overlapped craters are distributed on the EDMed surfaces. The size of the craters formed at various capacitances is evaluated quantitatively using a circle to surround the crater. At a voltage of 90 V and capacitance of 3300 pF, the diameter of the crater was determined to be about 13 μm, whereas they were about 8 μm and 5 μm for capacitances of 1000 pF and 220 pF, respectively. The smaller craters have positive effects on the surface quality, resulting in decreased surface roughness, as shown in Fig. 4.

Combining the surface morphologies shown in Fig. 5a–c, a similar conclusion can be derived from Fig. 6. At a capacitance of 3300 pF, the diameter of the crater decreased from about 17 μm to 11 μm when the voltage decreased from 110 V to 70 V, resulting in the decreased surface roughness seen in Fig. 4.

Results shown in Figs. 5 and 6 provide a reasonable explanation that decreased voltages and capacitances result in decreased surface roughness because of the decreased crater size. To explore the possible reason for the small impact of the voltage change on the surface roughness, for example, the results in Fig. 4b and e, Fig. 7 shows the surface morphology of the EDMed hole at a voltage of 110 V and capacitance of 1000 pF. At this condition, craters with a typical diameter of about 9 μm are formed, which are not very different from those in Fig. 5f obtained at a same capacitance but a decreased voltage of 90 V. Thus, a very similar surface roughness is obtained using the white-light interferometer. Another possible reason is related to the randomly overlapped distribution of craters, one crater present on top of the other. As shown in Figs. 5–7, the EDMed surfaces are distributed with a series of randomly overlapped craters. Some craters are complete while some are covered by the crater on the top surface. Hence, even though the crater size is the same, the surface roughness will be very different if the randomly overlapping process is different, resulting in various overlapped regions or depths. From this perspective, the measured surface roughness in Fig. 4 is a combined result of the crater size and the randomly overlapping process. When the crater size is greatly different, the surface roughness is mainly dependent of the crater size. When the crater size is similar, the randomly overlapped distribution of craters reduces the impact of individual crater sizes on the surface roughness.

In Fig. 4, it is noted that the center region is relatively smooth compared to the outer region. To address this, Fig. 8 presents the typical surface morphologies of the EDMed hole at a voltage of 70 V and capacitance of 220 pF. Surface microstructures at the outer region and around the center region are shown in detail in Fig. 8a and c, respectively. For comparative analysis, the same magnification (2000×) was selected. The difference between Fig. 8a and c is clear. In the outer region, individual craters can be identified in Fig. 8a, especially on the left side, which is closer to the edge of the EDMed hole. However, only small particles can be observed in the center region, as shown in Fig. 8c. Different microstructures in

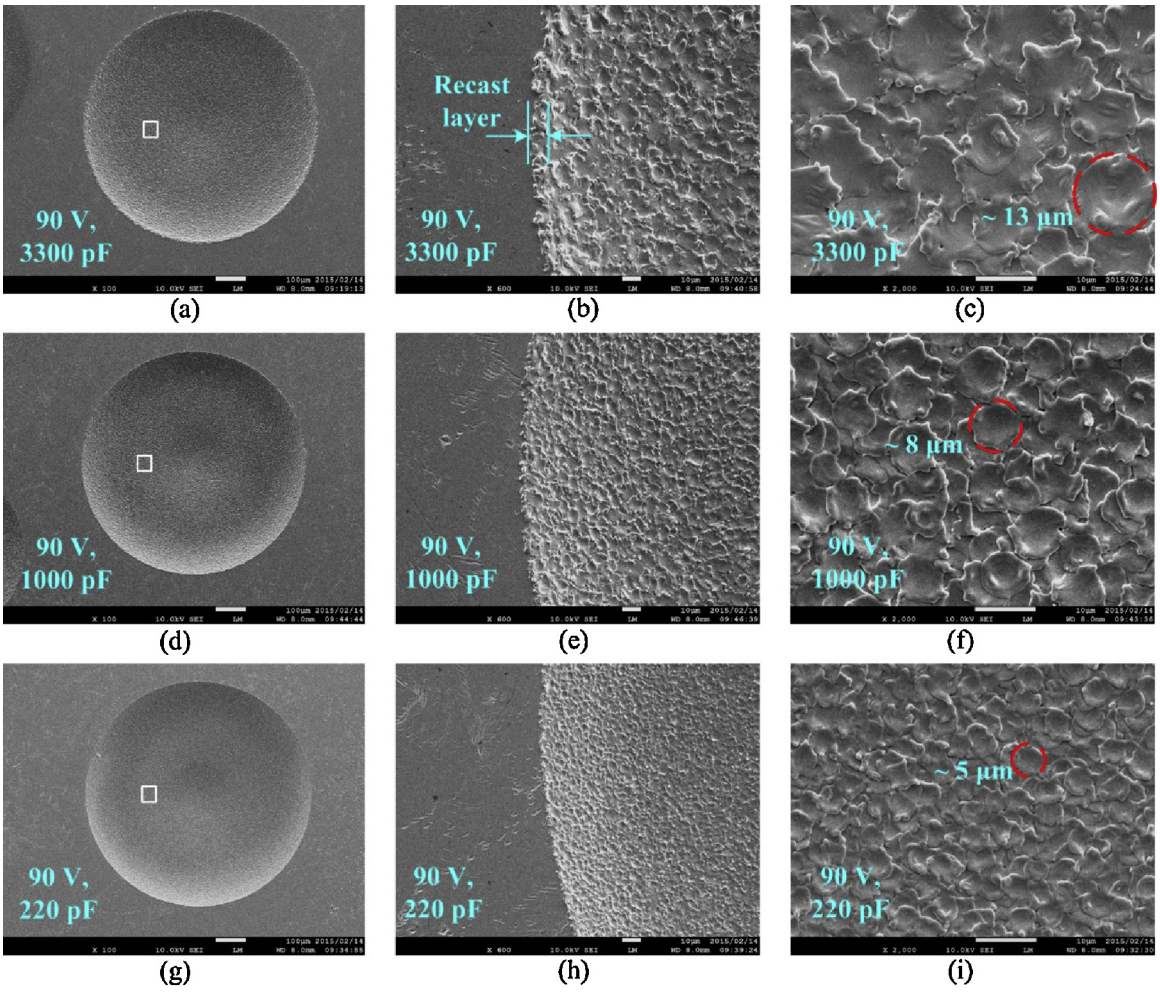

Fig. 5. Surface morphologies of the EDMed holes at a voltage of 90 V and various capacitances: (a)–(c) 3300 pF, (d)–(f) 1000 pF, (g)–(i) 220 pF.

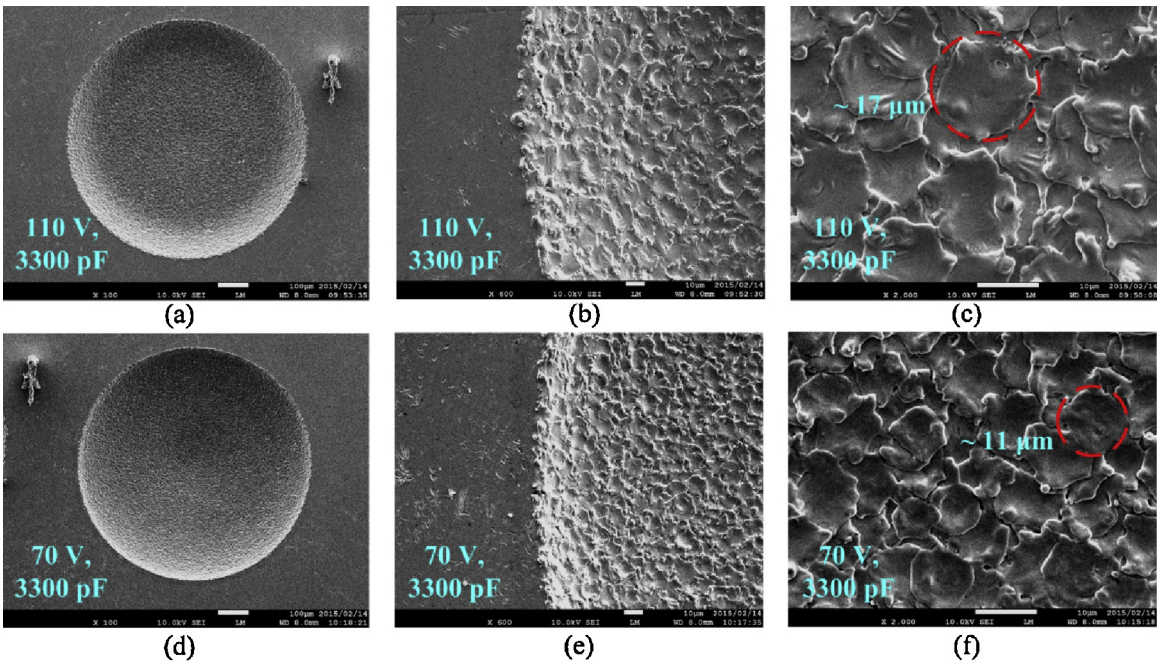

Fig. 6. Surface morphologies of the EDMed holes at a capacitance of 3300 pF and various voltages: (a)–(c) 110 V, (d)–(f) 70 V.

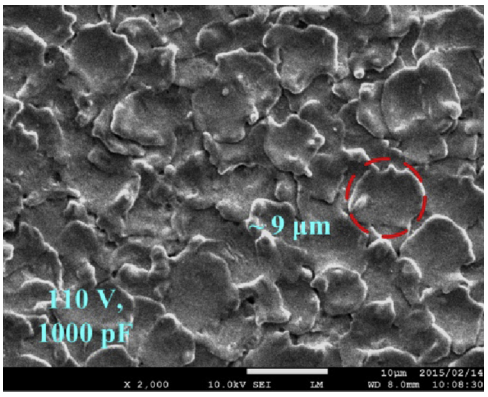

Fig. 7. Surface morphology of the EDMed hole at a voltage of 110 V and capacitance of 1000 pF.

the outer and center regions suggest different EDM processes due to various sparks, dielectric circulation, thermal dissipation, debris, etc.

3.5. Surface carbonization and crystallization

Because EDM oil, CASTY-LUBE EDS, was used as the dielectric fluid, the heat of sparking can break down this dielectric fluid into hydrogen, carbon, and other by-products during EDM. During the pulse-off time, carbon will be deposited on the EDMed surface. Fig. 9 shows the EDX results of the carbon distribution on the EDMed surface at 90 V and 3300 pF. Elemental carbon is distributed uniformly on the EDMed surface. Considering the high chemical affinity of C atoms with Zr and Ti atoms, these carbons may promote crystallization of the $Zr_{41.2}Ti_{13.8}Cu_{12.5}Ni_{10}Be_{22.5}$ BMG during EDM.

To characterize the carbon phase, micro-Raman spectra of the EDMed surfaces around the center regions at various voltages and capacitances were measured. Fig. 10 presents the typical Raman spectra of the EDMed surfaces at a voltage of 90 V and various capacitances. For voltages of 110 V and 70 V, similar Raman spectra were obtained (not shown here). In Fig. 10, two peaks at ~1350 cm^{-1} and 1580 cm^{-1} appear, commonly referred to as the G-peak and D-peak, respectively [38], further verifying the existence of elemental carbon. The wide shoulder at these two peaks indicates that the deposited carbon is amorphous rather than crystalline diamond or graphite, which show sharp peaks [38].

To explore the effects of the electro-thermal process and dissolved carbons on the surface crystallization of the BMG during micro-EDM, XRD patterns of the EDMed surfaces at a voltage of 70 V and various capacitances were obtained (Fig. 11). For comparative analysis, the XRD pattern of the as cast sample is also shown. Considering that different surface morphologies of the EDMed hole were obtained around the center and outer regions, as shown

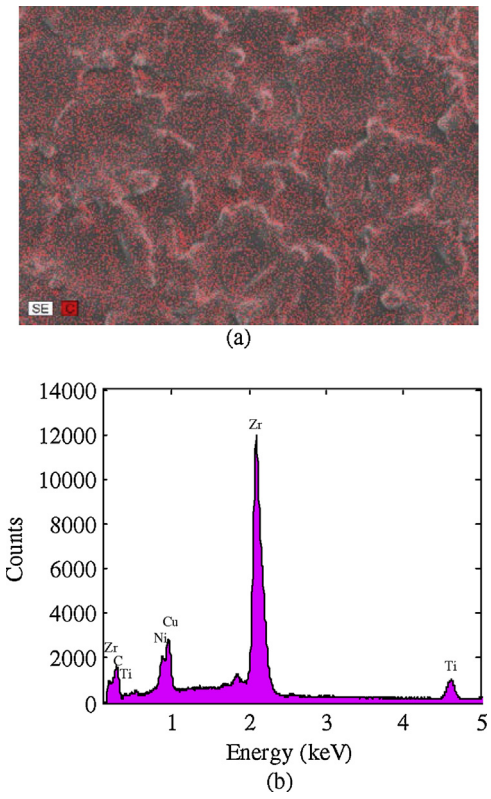

Fig. 9. (a) EDX results of carbon distribution on the EDMed surface at 90 V and 3300 pF, (b) EDX spectra.

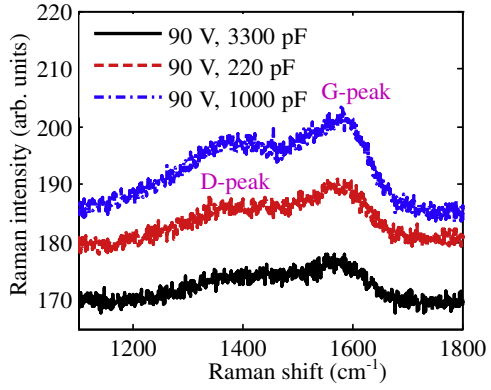

Fig. 10. Typical micro-Raman spectra of the EDMed surfaces at a voltage of 90 V and various capacitances.

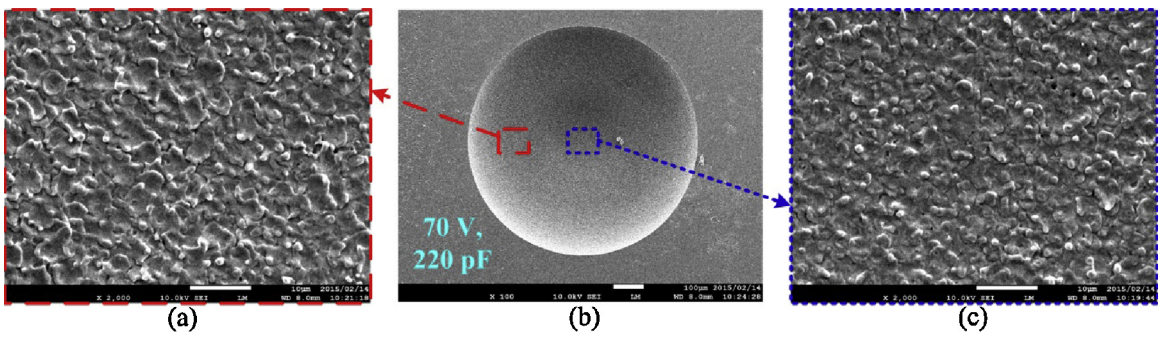

Fig. 8. Surface morphologies of the EDMed hole at a voltage of 70 V and capacitance of 220 pF: (a) the outer region, (b) the entire hole, (c) around the center region.

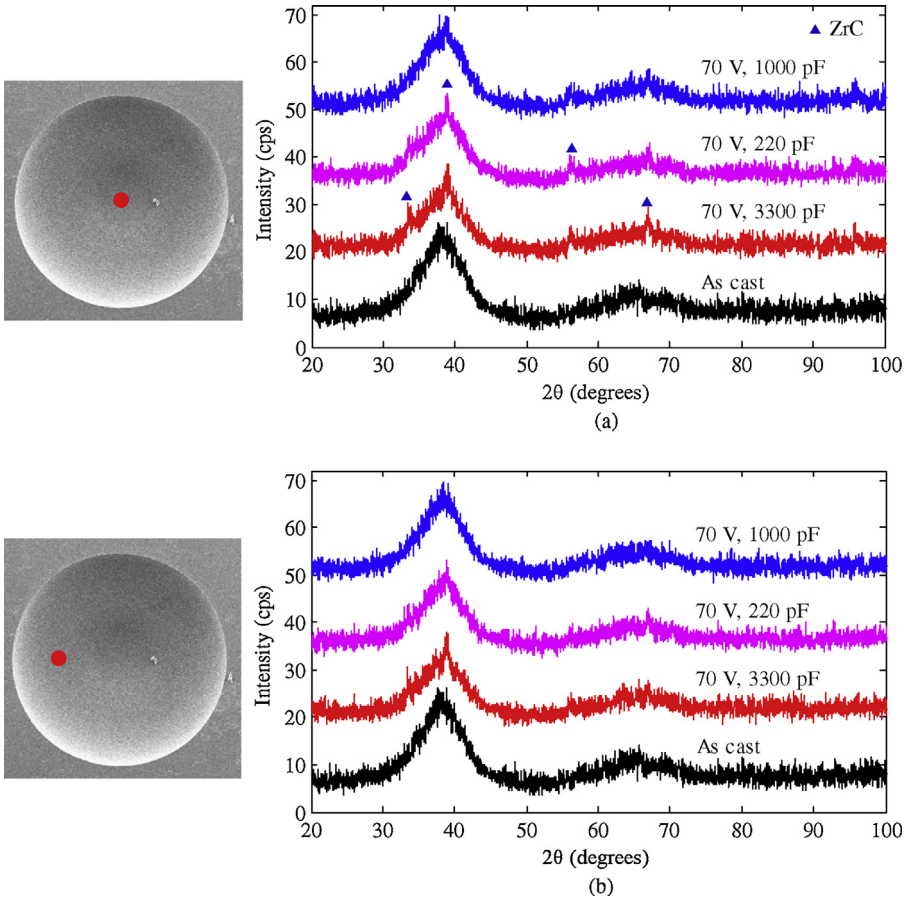

Fig. 11. XRD patterns of the EDMed surfaces at a voltage of 70 V and various capacitances: (a) around the center region and (b) the outer region.

in Fig. 8, XRD patterns around the center and outer regions are illustrated in Fig. 11a and b, respectively. Overall, a broad hump is observed in all XRD patterns of the EDMed surfaces, although there are some small peaks, demonstrating a dominant amorphous characteristic. Compared to the XRD pattern in Ref. [29], where many sharp peaks were observed on the surface of a Zr-based BMG machined by conventional EDM instead of the typically broad hump, results in Fig. 11 demonstrate a better ability to retain an amorphous structure during micro-EDM because of low discharge energy. According to the XRD software, these small peaks result from the formation of nanocarbides ZrC, leading to partial crystallization of the EDMed surfaces. Fig. 12 illustrates the partial crystallization mechanism of the EDMed surfaces. In Fig. 12a, sparks occur between the copper electrode and the Zr-based BMG during pulse-on. Some copper and BMG are molten, vaporized, and suspended in the EDM oil. Meanwhile, decomposed hydrogen and carbon are also suspended in the EDM oil. In some regions, vaporized BMGs and decomposed carbons may connect with each other, forming a mixture. During the pulse-off time, as shown in Fig. 12b, vaporized materials are re-solidified. Because of the high

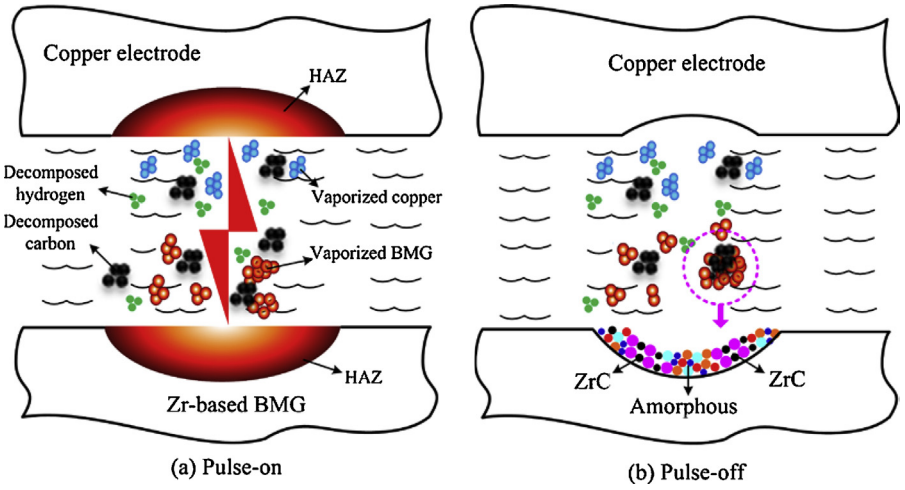

Fig. 12. (a) Pulse-on: electrode and workpiece material vaporized, and (b) pulse-off: vaporized materials re-solidified.

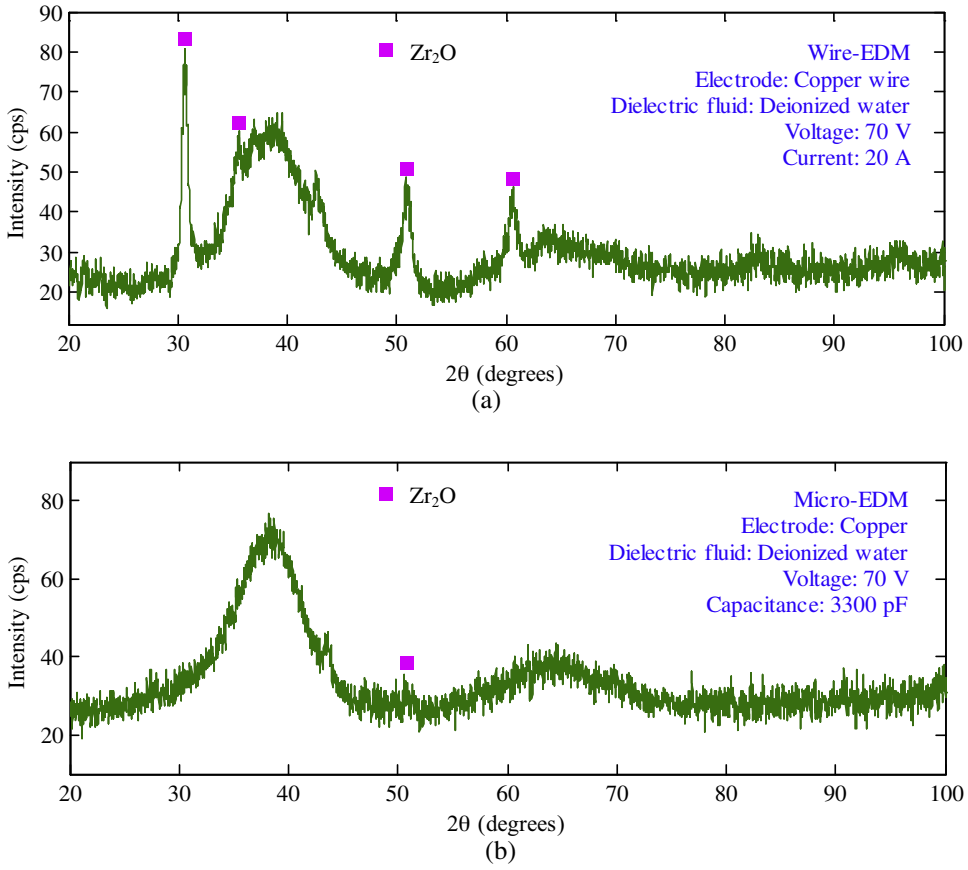

Fig. 13. XRD patterns of the surface machined by (a) conventional wire-EDM and (b) micro-EDM with deionized water.

chemical affinity of C atoms with Zr atoms, some nanocarbides ZrC are formed during the cooling and re-solidifying processes.

To address the role of decomposed carbon on the partial crystallization of the EDMed surfaces, the XRD pattern of the surface machined by conventional wire-EDM was obtained as shown in Fig. 13a. Experimental conditions are shown in this figure. Compared to the XRD patterns in Fig. 11, many sharp peaks appear in Fig. 13a, showing an obviously enhanced crystallization of the EDMed surface. To exclude the effect of various dielectrics on enhanced crystallization of the EDMed surface, Fig. 13b presents the XRD pattern of the surface machined by micro-EDM with deionized water, where only two very weak peaks appear. Results in Fig. 13 further confirm that micro-EDM with low discharge energy can retain a better amorphous structure of BMG. Furthermore, it is noted that the peak positions in Fig. 13 are different from those in Fig. 11, exhibiting different crystallization phases when deionized water was used where dissolved and decomposed oxygen existed. On the other hand, this also confirms the role of decomposed carbons on the partial crystallization of the EDMed surfaces in Fig. 11. Furthermore, the small peaks are inconspicuous in Fig. 11b compared to those in Fig. 11a, which implies that the outer region is less crystallized than the center. This further indicates that the outer and center regions experience different heating and cooling processes due to various sparks, dielectric circulation, thermal dissipation, debris, etc.

In Fig. 11, another phenomenon is noted. Peaks obtained on the surfaces machined at capacitances of 3300 pF and 220 pF are more conspicuous that those obtained on the surfaces machined

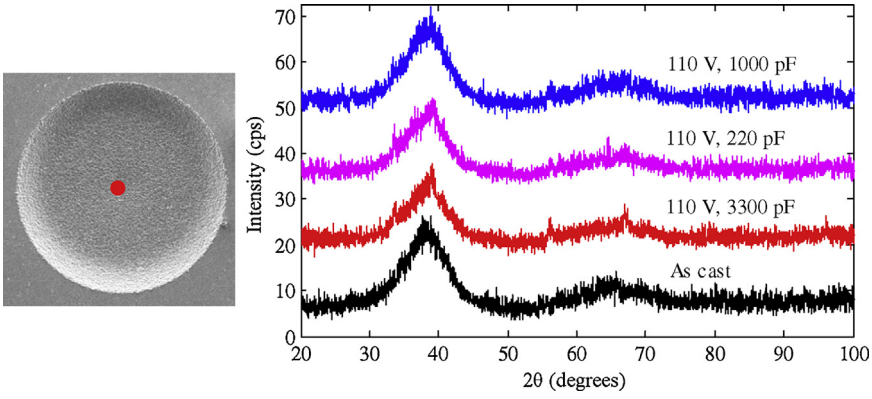

Fig. 14. XRD patterns around the center region of the EDMed surfaces at a voltage of 110 V and various capacitances.

at a capacitance of 1000 pF. In Fig. 11b, it is actually very difficult to identify the crystallization peaks in the XRD pattern obtained on the outer region of the EDMed surface at 70 V and 1000 pF, which exhibits a very similar XRD pattern to that obtained on the as cast sample surface. From the aspect of discharge energy, a large capacitance of 3300 pF induces a larger pulse energy and a longer discharge duration than those induced at a capacitance of 1000 pF, resulting in more heated, molten, and vaporized materials during pulse-on time. During pulse-off time, these heated materials are cooled, and the molten and vaporized materials are re-solidified. A large capacitance of 3300 pF produces a larger HAZ and more molten and vaporized materials, and thus, results in a lower cooling rate, leading to more significant crystallization than that at a capacitance of 1000 pF. For a smaller capacitance of 220 pF, much more time is consumed because of the relatively low pulse energy, and more thermal cycles and thermal accumulation are experienced in this case, which may be the reason leading to more conspicuous peaks than that at a capacitance of 1000 pF. From Fig. 11, it can be derived that for a given voltage, it is possible to reduce and even avoid crystallization of the EDMed surfaces by optimizing the capacitance.

To investigate the effects of the voltage on crystallization, Fig. 14 shows the XRD patterns around the center region of the EDMed surfaces at a voltage of 110 V and various capacitances. Similarly, the XRD pattern obtained on the surface machined at a capacitance of 1000 pF shows the weakest crystallization peaks. Compared to the XRD patterns obtained at a voltage of 70 V in Fig. 11, the EDMed surfaces of the BMG at a voltage of 110 V do not show enhanced crystallization peaks, indicating that voltage change from 70 V to 110 V has a small impact on the surface crystallization of the EDMed surfaces.

4. Conclusions

Micro-EDM machining performance of a Zr-based BMG was systematically investigated by orthogonal design of experiments. Effects of the discharge voltage and capacitance on the material removal rate, cross-sectional profile, surface morphology and roughness, carbonization, and crystallization of the EDMed surfaces were discussed. The main conclusions are summarized as follows:

(1) Experimental parameters exhibited a strong effect on the material removal rate, surface morphology, and surface roughness. Micro-EDM at low discharge voltages and capacitances produced smaller craters and recast layers, reduced the surface roughness but lowed the material removal rate.
(2) Amorphous carbons formed by the decomposition of EDM oil were deposited on the EDMed surfaces of the BMG. Some other carbons combined with Zr elements to form nanocarbides ZrC, leading to partial crystallization of the micro-EDMed surfaces.
(3) Compared to conventional EDM, the surfaces machined by micro-EDM retained better amorphous characteristic because of low discharge energy, showing very weak crystallization peaks in XRD patterns.
(4) Various dielectric fluids, EDM oil and deionized water, generated different decomposition products during pulse-on time, and thus formed different crystallization phases of the EDMed surfaces.
(5) The center and outer regions of the EDMed holes showed different microstructures and crystallization characteristics due to various sparks, dielectric circulation, thermal dissipation, debris, etc.
(6) For the capacitances used, 220 pF, 1000 pF, and 3300 pF, the EDMed surfaces machined at 1000 pF showed the weakest crystallization peaks; whereas a voltage change from 70 V to 110 V had a small impact on the surface crystallization.

Acknowledgments

H.H. is an International Research Fellow of the Japan Society for the Promotion of Science (JSPS). This study has been financially supported by Grant-in-Aid for JSPS Fellows (Grant No. 26-04048). Authors also give thanks to Dr. Zhiwei Zhu at the Hong Kong Polytechnic University for providing the bulk metallic glass sample and to Kazunori Watanabe and Tsong Han Tan at Keio University for technical support during EDM experiments.

References

[1] J. Plummer, W.L. Johnson, Is metallic glass poised to come of age? Nat. Mater. 14 (2015) 553–555.
[2] J. Schroers, W.L. Johnson, Ductile bulk metallic glass, Phys. Rev. Lett. 93 (2004) 255506.
[3] C.A. Schuh, T.C. Hufnagel, U. Ramamurty, Overview no.144 – mechanical behavior of amorphous alloys, Acta Mater. 55 (2007) 4067–4109.
[4] Y.H. Liu, G. Wang, R.J. Wang, D.Q. Zhao, M.X. Pan, W.H. Wang, Super plastic bulk metallic glasses at room temperature, Science 315 (2007) 1385–1388.
[5] W.H. Wang, Roles of minor additions in formation and properties of bulk metallic glasses, Prog. Mater. Sci. 52 (2007) 540–596.
[6] W.H. Wang, C. Dong, C.H. Shek, Bulk metallic glasses, Mater. Sci. Eng. R 44 (2004) 45–89.
[7] W.H. Wang, The elastic properties, elastic models and elastic perspectives of metallic glasses, Prog. Mater. Sci. 57 (2012) 487–656.
[8] M. Bakkal, C.T. Liu, T.R. Watkins, R.O. Scattergood, A.J. Shih, Oxidation and crystallization of Zr-based bulk metallic glass due to machining, Intermetallics 12 (2004) 195–204.
[9] M. Bakkal, A.J. Shih, S.B. McSpadden, C.T. Liu, R.O. Scattergood, Light emission, chip morphology, and burr formation in drilling the bulk metallic glass, Int. J. Mach. Tools Manuf. 45 (2005) 741–752.
[10] M. Bakkal, A.J. Shih, S.B. McSpadden, R.O. Scattergood, Thrust force, torque, and tool wear in drilling the bulk metallic glass, Int. J. Mach. Tools Manuf. 45 (2005) 863–872.
[11] M. Bakkal, A.J. Shih, R.O. Scattergood, Chip formation, cutting forces, and tool wear in turning of Zr-based bulk metallic glass, Int. J. Mach. Tools Manuf. 44 (2004) 915–925.
[12] M. Bakkal, A.J. Shih, R.O. Scattergood, C.T. Liu, Machining of a Zr–Ti–Al–Cu–Ni metallic glass, Scr. Mater. 50 (2004) 583–588.
[13] K. Fujita, Y. Morishita, N. Nishiyama, H. Kimura, A. Inoue, Cutting characteristics of bulk metallic glass, Mater. Trans. 46 (2005) 2856–2863.
[14] M.Q. Jiang, L.H. Dai, Formation mechanism of lamellar chips during machining of bulk metallic glass, Acta Mater. 57 (2009) 2730–2738.
[15] N.U. Tariq, G. Muhammad, H. Bin Awais, Effect of operating parameters on the drilling behavior of $Zr_{57.5}Cu_{11.2}Ni_{13.8}Al_{17.5}$ bulk metallic glass, J. Mater. Res. 28 (2013) 3288–3296.
[16] J. Schroers, The superplastic forming of bulk metallic glasses, JOM (U.S.) 57 (2005) 35–39.
[17] G. Kumar, H.X. Tang, J. Schroers, Nanomoulding with amorphous metals, Nature 457 (2009) 868–872.
[18] W.L. Johnson, G. Kaltenboeck, M.D. Demetriou, J.P. Schramm, X. Liu, K. Samwer, C.P. Kim, D.C. Hofmann, Beating crystallization in glass-forming metals by millisecond heating and processing, Science 332 (2011) 828–833.
[19] G. Kaltenboeck, T. Harris, K. Sun, T. Tran, G. Chang, J.P. Schramm, M.D. Demetriou, W.L. Johnson, Accessing thermoplastic processing windows in metallic glasses using rapid capacitive discharge, Sci. Rep. (U.K.) 4 (2014) 6441.
[20] Y. Saotome, K. Itoh, T. Zhang, A. Inoue, Superplastic nanoforming of Pd-based amorphous alloy, Scr. Mater. 44 (2001) 1541–1545.
[21] Y. Saotome, K. Imai, S. Shioda, S. Shimizu, T. Zhang, A. Inoue, The micro-nanoformability of Pt-based metallic glass and the nanoforming of three-dimensional structures, Intermetallics 10 (2002) 1241–1247.
[22] A. Wiest, J.S. Harmon, M.D. Demetriou, R.D. Conner, W.L. Johnson, Injection molding metallic glass, Scr. Mater. 60 (2009) 160–163.
[23] J. Schroers, Q. Pham, A. Peker, N. Paton, R.V. Curtis, Blow molding of bulk metallic glass, Scr. Mater. 57 (2007) 341–344.
[24] J. Schroers, Processing of bulk metallic glass, Adv. Mater. 22 (2010) 1566–1597.
[25] G. Kumar, A. Desai, J. Schroers, Bulk metallic glass: the smaller the better, Adv. Mater. 23 (2011) 461–476.
[26] Z.Y. Zhang, H.M. Peng, J.W. Yan, Micro-cutting characteristics of EDM fabricated high-precision polycrystalline diamond tools, Int. J. Mach. Tools Manuf. 65 (2013) 99–106.
[27] J.W. Yan, K. Watanabe, T. Aoyama, Micro-electrical discharge machining of polycrystalline diamond using rotary cupronickel electrode, CIRP Ann. Manuf. Technol. 63 (2014) 209–212.

[28] P.J. Liew, J.W. Yan, T. Kuriyagawa, Experimental investigation on material migration phenomena in micro-EDM of reaction-bonded silicon carbide, Appl. Surf. Sci. 276 (2013) 731–743.
[29] S.F. Hsieh, S.L. Chen, M.H. Lin, S.F. Ou, W.T. Lin, M.S. Huang, Crystallization and carbonization of an electrical discharge machined Zr-based bulk metallic glass alloy, J. Mater. Res. 28 (2013) 3177–3184.
[30] S.H. Yeo, P.C. Tan, E. Aligiri, S.B. Tor, N.H. Loh, Processing of zirconium-based bulk metallic glass (BMG) using microelectrical discharge machining (micro-EDM), Mater. Manuf. Process. 24 (2009) 1242–1248.
[31] X.H. Chen, X.C. Zhang, Y. Zhang, G.L. Chen, Fabrication and characterization of metallic glasses with a specific microstructure for micro-electro-mechanical system applications, J. Non-Cryst. Solids 354 (2008) 3308–3316.
[32] A. Peker, W.L. Johnson, A highly processable metallic-glass – $Zr_{41.2}Ti_{13.8}Cu_{12.5}Ni_{10.0}Be_{22.5}$, Appl. Phys. Lett. 63 (1993) 2342–2344.
[33] H.A. Bruck, T. Christman, A.J. Rosakis, W.L. Johnson, Quasi-static constitutive behavior of $Zr_{41.25}Ti_{13.75}Ni_{10}Cu_{12.5}Be_{22.5}$ bulk amorphous-alloys, Scr. Metall. Mater. 30 (1994) 429–434.
[34] H.A. Bruck, A.J. Rosakis, W.L. Johnson, The dynamic compressive behavior of beryllium bearing bulk metallic glasses, J. Mater. Res. 11 (1996) 503–511.
[35] A. Masuhr, T.A. Waniuk, R. Busch, W.L. Johnson, Time scales for viscous flow, atomic transport, and crystallization in the liquid and supercooled liquid states of $Zr_{41.2}Ti_{13.8}Cu_{12.5}Ni_{10.0}Be_{22.5}$, Phys. Rev. Lett. 82 (1999) 2290–2293.
[36] J.Z. Jiang, T.J. Zhou, H. Rasmussen, U. Kuhn, J. Eckert, C. Lathe, Crystallization in $Zr_{41.2}Ti_{13.8}Cu_{12.5}Ni_{10}Be_{22.5}$ bulk metallic glass under pressure, Appl. Phys. Lett. 77 (2000) 3553–3555.
[37] C.C. Aydiner, E. Ustundag, M.B. Prime, A. Peker, Modeling and measurement of residual stresses in a bulk metallic glass plate, J. Non-Cryst. Solids 316 (2003) 82–95.
[38] E. Shibata, R. Sergiienko, H. Suwa, T. Nakamura, Synthesis of amorphous carbon particles by an electric arc in the ultrasonic cavitation field of liquid benzene, Carbon 42 (2004) 885–888.